CYCLIC TEST ON A PRECAST REINFORCED CONCRETE COLUMN-TO-FOUNDATION GROUTED DUCT CONNECTION

Nerio TULLINI[a], Fabio MINGHINI[b]

Engineering Department, University of Ferrara, Via Saragat 1, Ferrara, Italy

[a] Corresponding author. E-mail: nerio.tullini@unife.it; Phone: +39 (0) 532 974936

[b] E-mail: fabio.minghini@unife.it

ABSTRACT

A full-scale specimen of a column-to-foundation grouted duct connection suited for buildings and industrial structures is tested in cyclic bending combined with axial compression. The positioning of the steel ducts along the sides of the column cross-section allows for using traditional reinforcement cages for the column, with longitudinal bars at both mid-side and corners of the cross-section. Splice length and amount of transverse reinforcement along the splice are defined based on Eurocode 2 provisions for laps of reinforcing bars. A discussion on dissipated energy, connection strength and ductility is reported. The hysteretic energy dissipated by the connection is close to that reported in the literature for a cast-in-place specimen of comparable capacity pushed up to the same maximum drift. With respect to the design values of bending resistance and curvature ductility computed for traditional reinforced concrete sections, the joint section shows an over-strength factor of 1.4 and a gain in ductility of 87%.

Keywords: Precast concrete column; Column-to-foundation connection; Grouted duct connection; Cyclic test; Ductility

1. INTRODUCTION

In precast Reinforced Concrete (RC) construction, the connection behavior influences the overall structural response considerably (Elliot 2017), specifically in precast structures subjected to

earthquake loading. In fact, when they are inadequate, catastrophic failure may occur, as was testified by the evidence of past earthquakes (Yanev 1989; Sezen and Whittaker 2006; Toniolo and Colombo 2012; Belleri et al. 2015; Minghini et al. 2016; Savoia et al. 2017; Buratti et al. 2017) and demonstrated by recent numerical investigations (Demartino et al. 2018). The scientific community is then becoming much sensitive to the need for developing innovative connection systems with strength and ductility suitable to resist earthquakes (Negro and Toniolo 2012).

Grouted joints are gaining increasing importance for use in earthquake resistant structures made of precast RC. They can be designed to develop strength and ductility comparable with those of cast-in-place connections and offer the advantage of a significant speed of assembly. Among the connection types based on splicing of the longitudinal reinforcement, two main categories can be identified: (1) connections using bar couplers and (2) grouted duct connections.

The connections using bar couplers (Hua et al. 2014; Yuan et al. 2017; Liu et al. 2018; Yan et al. 2018) allow the tensile load to be transferred from one bar to another bar collinear to the first one. The spliced bars are inserted into a metal sleeve that must be grouted to make the connection operational. The couplers are generally made of mild steel, but also aluminium sleeves have been proposed, such as the specimens of the AS series tested by Hua et al. (2014). The overall length and outer diameter of grouted couplers generally do not exceed $20\varnothing_b$ and $4\varnothing_b$, respectively, with $\varnothing_b$ being the diameter of the spliced bar. The tensile capacity of the connection is ensured by the confining effect offered by the sleeve to the grout inside it, and by the grout to the spliced bars (Hua et al. 2014). In column-to-foundation connections, the bar couplers can be placed inside the footing or, alternatively, in the column base (Ameli et al. 2016). In both cases, global ductility is generally lower than that allowed by cast-in-place concrete construction, but, anyway, is generally adequate for use in moderate-to-high seismic zones. When the couplers are placed in the column base, the loss in ductility is attributed to the disruption introduced by the couplers to the plastic hinge zone of the column. However, damage localization at the column-foundation interface occurs, allowing for a relatively simple and fast retrofitting. Alternative types of couplers are represented by threaded

mechanical connectors. Cyclic load test results on a column-to-foundation joint using such connectors were recently presented by Dal Lago et al. (2016). Compared to monolithic solutions, the energy dissipation of this joint was smaller due to pinching in the hysteretic response, but the effective plastic hinge length was substantially the same.

Grouted duct connections make use of non-contact lap splices of the longitudinal reinforcement (Park 1995; FIB 2003; Rave-Arango et al. 2018). The bars protruding from one precast unit are grouted into corrugated steel ducts encased in the other unit. Adjacent to each duct one or more bars are present, lap-spliced to the outside of the duct. The experimental analyses conducted by Kuttab and Dougill (1988) and Zheng (1996) should be mentioned among the first researches on column-to-column grouted duct connections. Similar connections, but specifically tailored to column-to-foundation joints, were proposed and tested by Belleri and Riva (2012) and, more recently, by Popa et al. (2015) in very interesting research papers. In these connections, analogous to that illustrated in Fig. 5-35 of FIB Bulletin No. 27 (FIB 2003), four projecting bars, embedded in the footing and protruding from it, are inserted into just as many corrugated steel ducts placed at the corners of the column cross-section and then grouted. Two smaller-diameter bars are placed in the column adjacent to each duct. The lap splice of the projecting and smaller-diameter bars enables the load transfer mechanism between column and footing. A similar connection system, specifically suited for buildings and industrial structures, was recently proposed by Tullini and Minghini (2016) for column-to-column joints. In that proposal, however, the steel ducts were positioned along the sides of the column cross-section rather than at the corners, so allowing for the use of traditional reinforcement cages presenting longitudinal bars at both mid-side and corners of the cross-section. The reader is referred to Fig. 1 for a comparison between the connections tested by Zheng (1996), Belleri and Riva (2012), Popa et al. (2015) and Tullini and Minghini (2016). The connection was tested in tension, monotonic and cyclic bending with zero axial load, monotonic bending combined with axial compression and cyclic shear.
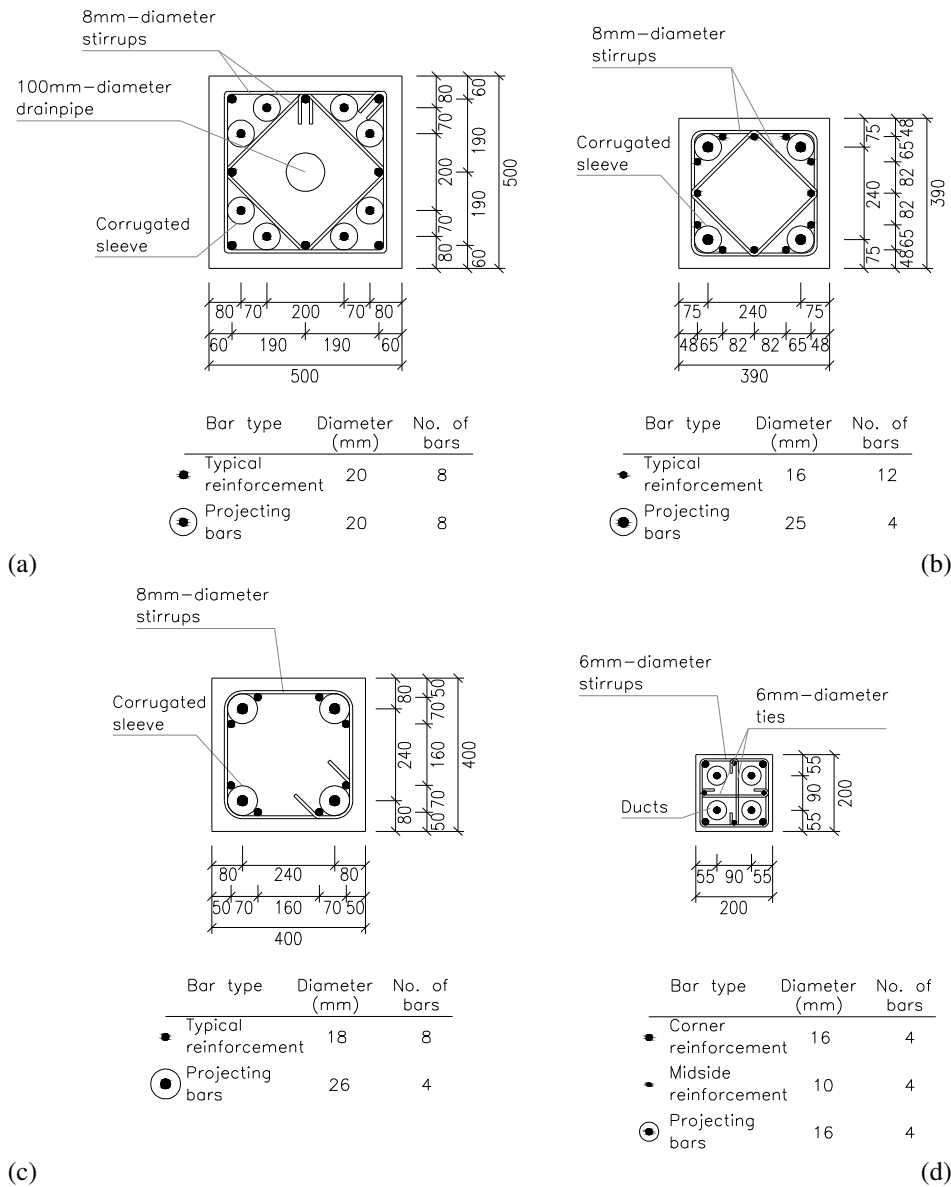
Fig. 1 Comparison between different grouted connections: typical column cross-section in the lap splice region for the connection systems proposed by (a) Tullini and Minghini (2016), (b) Popa et al. (2015), (c) Belleri and Riva (2012) and (d) Zheng (1996). Dimensions in mm

The aim of the present paper is to carry through with the experimental investigation of the connection system proposed by Tullini and Minghini (2016). The same system, indeed, has been used for a column-to-foundation joint and subjected to cyclic bending combined with axial compression. The adopted test configuration is analogous to that referred to as Case IV in user's manual of database provided by Pacific Earthquake Engineering Research Center (PEER 2004), with the axial load not passing through the intersection between column centreline and footing. The relevant test results, followed by considerations on ductility and dissipated energy, are reported

hereinafter. In addition to the measurements of transverse deflection and longitudinal displacements at the column base, usually adopted in analogous tests to compute average strains and curvature (Belleri and Riva 2012), the shear slip at the column-foundation interface was measured during the test. The slip measurement was accounted for in evaluating the influence of second order effects, resulting in a modified expression for the axial load eccentricity with respect to that deduced from PEER Center's manual (PEER 2004). Being the cyclic response of cast-in-place column-to-foundation joints widely consolidated in the literature (Belleri and Riva 2012; Popa et al. 2015; Liu et al. 2018), it was chosen not to repeat the experimental test on an analogous cast-in-place connection.

2. DESCRIPTION OF THE COLUMN-TO-FOUNDATION CONNECTION

The full-scale test specimen is depicted in Fig. 2. The 3.7 m-long precast column (Fig. 2a) is connected with a 500 mm-thick foundation showing in plan dimensions 1.74×1.20 m (Fig. 2b). The column has a square cross-section with the side of 500 mm.

Two HEB 500 steel profiles are used to delimit the footing along the shortest edges, allowing for the installation into the reaction frame. The footing principal reinforcement, parallel to the bending plane adopted in the test, is comprised of two layers of 20 mm-diameter bars welded to the webs of the steel profiles. Two layers of 16 mm-diameter bars are used in the orthogonal direction. The eight projecting bars, protruding from the foundation, have the diameter of 20 mm.

The most significant column cross-sections are depicted in Fig. 2b. The regular reinforcement is comprised of eight 20 mm-diameter bars positioned at mid-side and corners of the cross-section (cross-section D-D in Fig. 2b). The clear concrete cover is 42 mm, leading to a distance of the centroidal axis of the regular reinforcement to the concrete surface of 60 mm. Eight corrugated steel ducts, with outer diameter and thickness of 63 and 0.8 mm, respectively, are encased in the column to allow for the insertion of the projecting bars protruding from the foundation. The ducts are bent

toward the lateral column surface so as to allow for grouting. The lap splice, enabling the stress transfer between projecting bars and regular column reinforcement, has the length of 1 m (Fig. 2a).
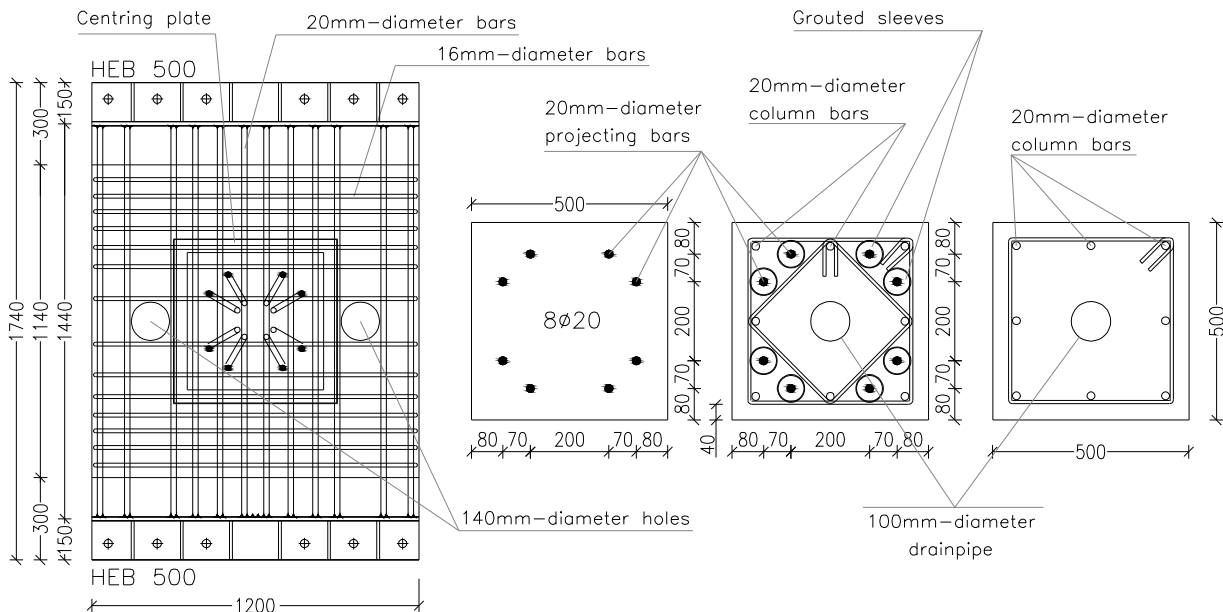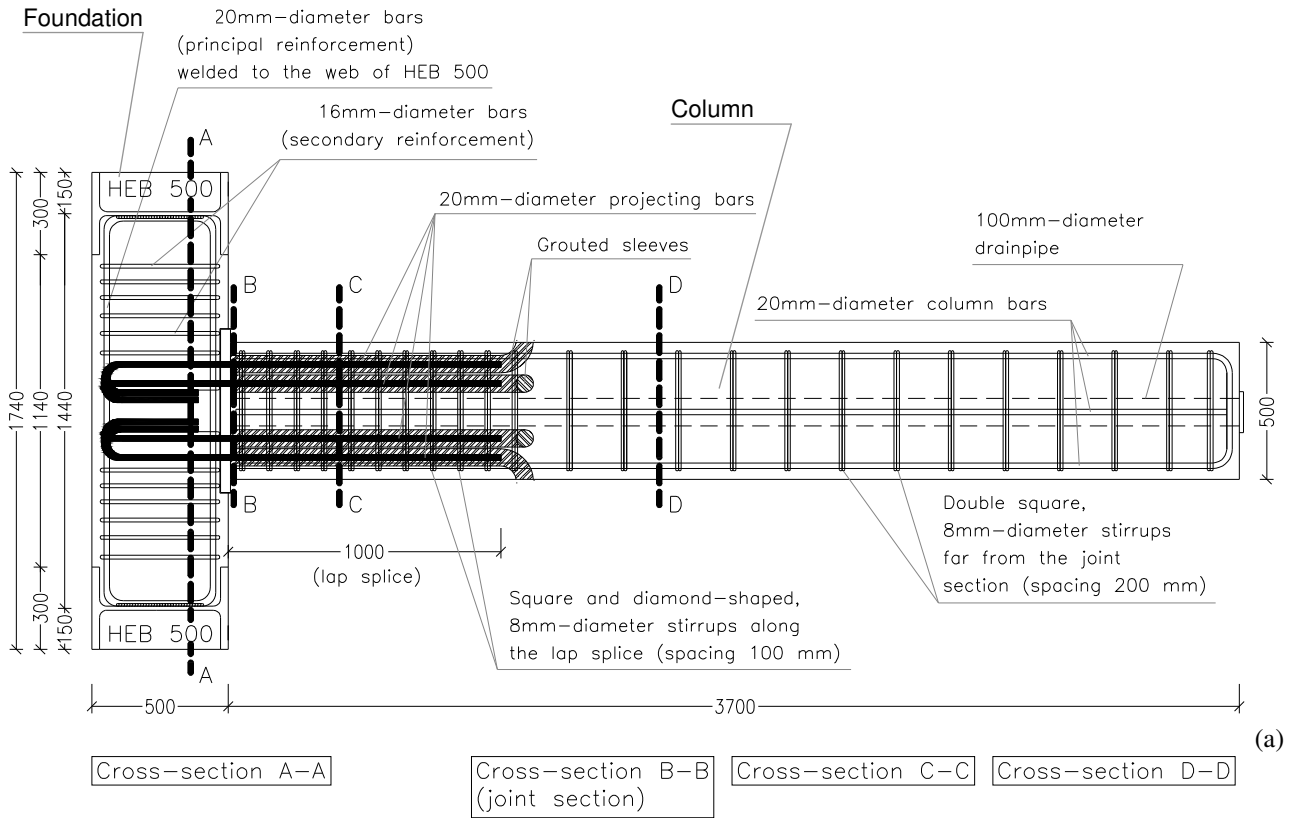

Fig. 2 Specimen used for the cyclic load test on the column-to-foundation connection: (a) side view of the reinforcement details and (b) relevant cross-sections. Dimensions in mm

The transverse column reinforcement is comprised of 100 mm-spaced square and diamond-shaped stirrups along the lap splice (cross-section C-C in Fig. 2b) and 200 mm-spaced pairs of square stirrups outside the lap zone. All stirrups are obtained from 8 mm-diameters deformed bars. The cross-section at the column-foundation interface (cross-section B-B in the Fig. 2b) is characterized by the presence of the eight projecting bars only. This section will be referred to as the joint section. The minimum distance from the centroidal axis of the projecting bars to the concrete surface is of 80 mm.

Detail views of the reinforcement cages of footing and column are shown in Figs. 3a and 3b, respectively. In Fig. 3a, the projecting bars can be observed. The two PVC tubes placed into the cage, having the diameter of 140 mm, serve to create holes through the footing, that will accommodate the Dywidag bars used for post-tensioning (see Sect. 4.3.1). In Fig. 3b, the steel ducts and reinforcement details in the lap zone can be observed. The assembled specimen, with the ducts just grouted, is shown in Figs. 3c.
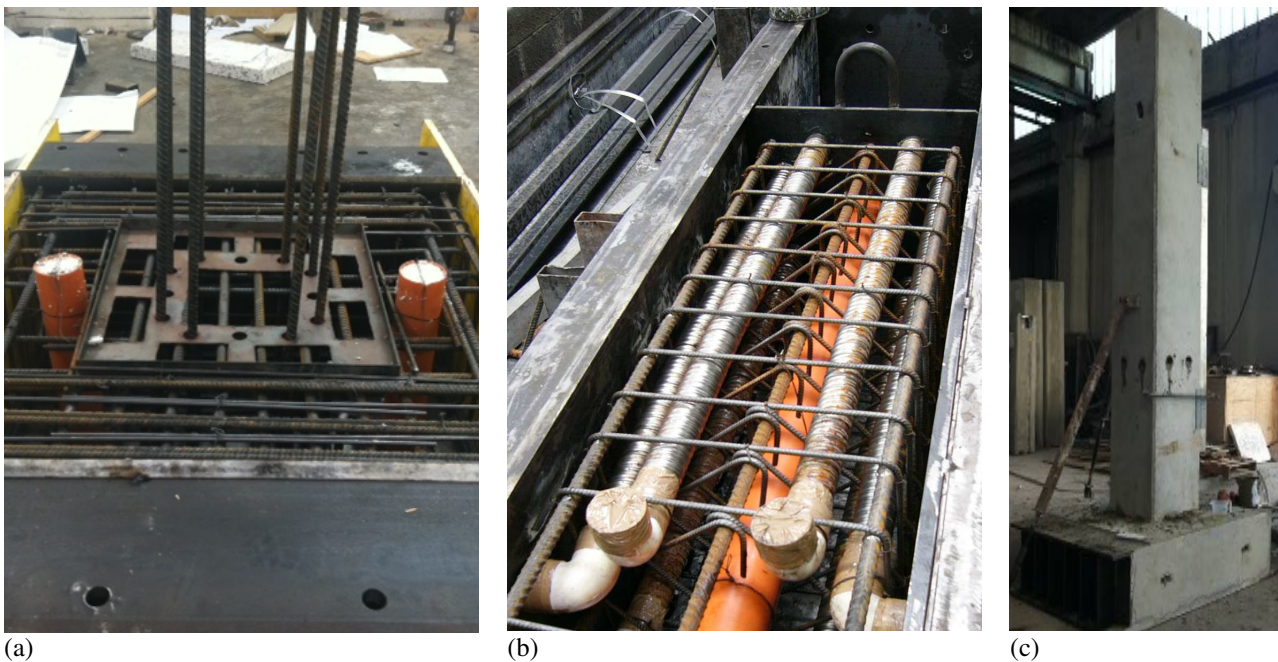

(a) (b) (c)

Fig. 3 Reinforcement cages of (a) foundation, with the eight projecting bars, and (b) column, with the corresponding corrugated steel sleeves; (c) assembled specimen with the sleeves just grouted

2.1. Design of the lap splice

The lap splice of the longitudinal column reinforcement (projecting and regular 20 mm-diameter bars) was designed based on Eurocode 2 provisions (CEN 2004a) for traditional deformed bars. The calculation of the lap splice length based on concrete strength class C40/50 is summarized in the Appendix. The design lap lengths for tension and compression result to be $l_{0t} = 897$ mm and $l_{0c} = 828$ mm, corresponding to 45 $\varnothing_b$ and 41 $\varnothing_b$, respectively. Neglecting the confining effect exerted by the metal ducts on the injection grout, and then on the projecting bars, a lap length $l_0 \geq \max\{l_{0t}, l_{0c}\}$ should be adopted. The actual lap length of 1 m, corresponding to 50 $\varnothing_b$, satisfies such requirement. For the grouted duct connection shown in Fig. 6.1 reported by Bruggeling and Huyghe (1991), similar to those proposed by FIB (2003), Belleri and Riva (2012) and Popa et al. (2015), the recommended lap splice length between each of the projecting bars placed at the corners of the cross-section and the two bars adjacent to each metal duct is of 40 $\varnothing_b$.

With regard to the transverse reinforcement, along each of the two end regions of the lap splice of length $l_0/3 = 333$ mm, each regular longitudinal bar is engaged by 4 stirrups, i.e., the total area of stirrups at the lap end regions satisfies the requirement $\Sigma A_{st} \geq A_s$ (CEN 2004a), with $A_s = 314$ mm^2 being the cross-sectional area of one single spliced bar (see the Appendix).

3. MATERIAL PROPERTIES

3.1. Concrete

During each of the days scheduled for casting the column and footing, 150 mm cubes were moulded to be tested in compression. Two cubes were prepared from each of the concrete mixes used for the precast units. In addition, two cubes were prepared from the concrete mix adopted for the injection grout. All cubes were tested in compression just before the cyclic test on the column-to-foundation connection. For each pair of cubes, the mean value $f_{cm,cube}(t)$ of the compressive strength at a concrete age t, variable from pair to pair, and the corresponding value $f_{cm,cube}(28) = f_{cm,cube}(t)/\beta_{cc}(t)$

at $t = 28$ days are given in Table 1, where coefficient $\beta_{cc}(t)$ is computed in accordance with Eurocode 2 (CEN 2004a). The concrete strengths for column and foundation allow for referring, in design calculations, to strength class C40/50 (characteristic cylinder strength $f_{ck} = 40$ MPa), which is the minimum of the classes reported in Eurocode 2 (CEN 2004a) that are compatible with the measured strengths.

3.2. Reinforcing steel

The mechanical properties of reinforcing steel were estimated based on tension tests on 20 mm- and 8 mm-diameter bars used for longitudinal and transverse reinforcement, respectively. Three steel specimens were tested for each diameter. The mean values of the obtained properties are given in Table 2. These properties are consistent with steel class B450C recommended by the Italian standard (IMIT 2018), showing yield and ultimate design strengths $f_{yd} = f_{yk}/\gamma_s = 450/1.15 = 391$ MPa and $f_{td} = f_{tk}/\gamma_s = 540/1.15 = 470$ MPa.

Table 1 Concrete and grout compressive strengths obtained from tests on cubic specimens

Concrete type	Concrete age, t [days]	$\beta_{cc}(t)$	$f_{cm,cube}(t)$ [MPa]	$f_{cm,cube}(28)$ [MPa]
Foundation	81	1.086	62.2	57.3
Column	77	1.083	61.3	56.6
Grout	75	1.081	70.8	65.5

Table 2 Mean values of mechanical properties for reinforcing steel

Bar diameter [mm]	E_{sm} [GPa]	f_{ym} [MPa]	f_{tm} [MPa]	f_{tm}/f_{ym}	ε_{tm} [%]
8	Not available	518	616	1.19	11
20	198	556	665	1.20	11

4. CYCLIC TEST ON THE COLUMN-TO-FOUNDATION CONNECTION

In this Section, the results obtained from a quasi-static cyclic test on the column-to-foundation connection are reported. Quasi-static load testing is one of the mostly used experimental methods to assess performance and available ductility during major earthquakes (Park 1988).

Test layout, loading protocol, equipment and measuring systems are described in detail hereinafter. The experimental results are followed by an analytical interpretation of the cyclic response of the joint section.

4.1. Specimen layout

The specimen was placed on the reaction frame horizontally as shown in Fig. 4a. The cyclic load direction was belonging to the vertical plane. This load was applied to the column at $L_\Delta = 2.8$ m from the joint section. Axial compression, N, was applied to the column end section. This configuration, analogous to Case IV described in PEER Center's manual (PEER 2004), is frequently adopted for cyclic load tests (Verderame et al. 2008a, b; Buratti et al. 2014).

The test layout at the initial, undeformed stage is illustrated in Fig. 5a, where the specimen is represented in grey. Assuming that a slip at the column-foundation interface may take place combined with column deflection, the generic specimen configuration during the test can be represented as the schematic of Fig. 5b, where:

- line *OEE'* represents the undeformed column axis (for clarity, points *E* and *E'* are also reported in Fig. 5a);

- line *ACC'* represents the column axis translated upward of generic quantity *s*;

- segment *DAE* corresponds to column-foundation interface;

- quantities *e* and *s* represent axial load eccentricity and interface slip between column and foundation, respectively;

- line *ABB'* is the column axis at a generic stage during the test. In representing this inclined straight line, it was assumed that the elastic flexural deformation of the column is negligible compared with
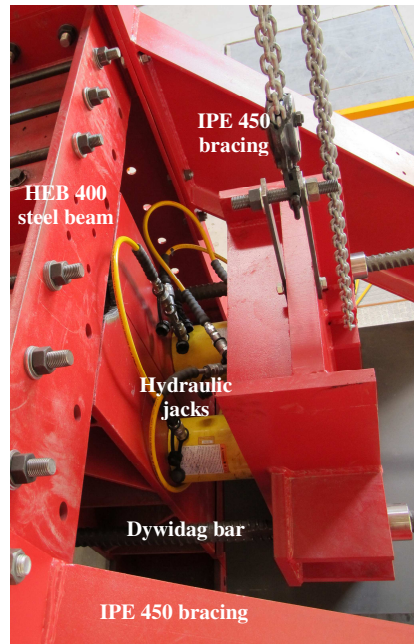
inelastic shear-flexural deformation which will occur at the joint section; this is an usual assumption (PEER 2004, Verderame et al. 2008a);
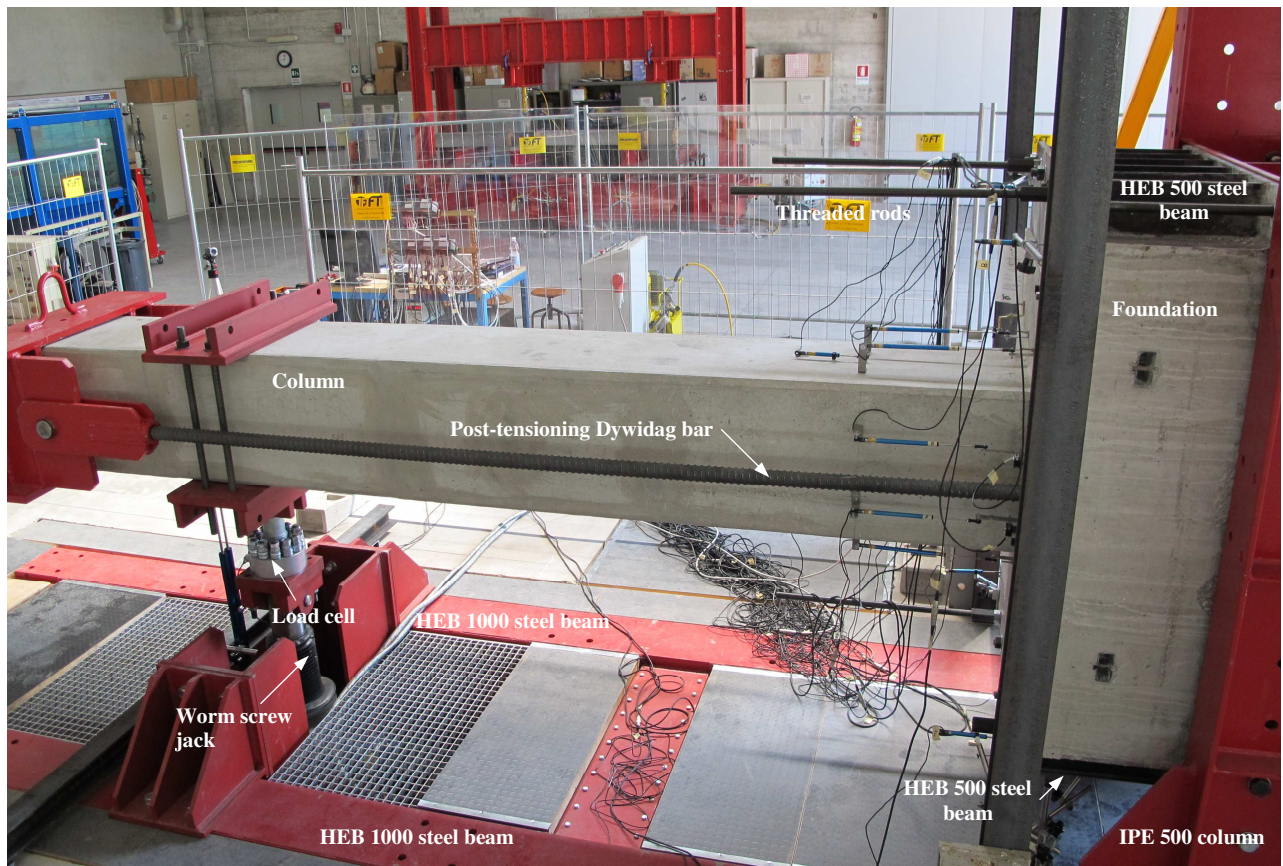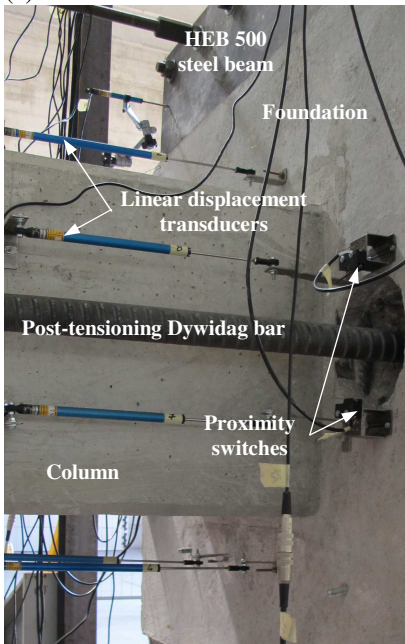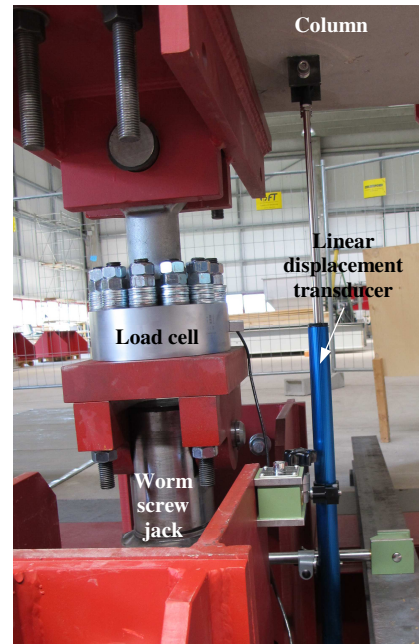
Fig. 4 Specimen installed into the reaction frame: (a) side view; detail views showing (b) the column-to-foundation connection with one of the Dywidag bars for post-tensioning and linear displacement transducers for strain measurements, (c) the two hydraulic jacks used to apply the constant axial load, and (d) the worm screw jack used to apply the cyclic transverse force

Fig. 5 Specimen layout: (a) side view (specimen in grey) and schematic for the evaluation of (b) second order effects due to N and of (c) deflection Δ based on measured deflection u_{18}

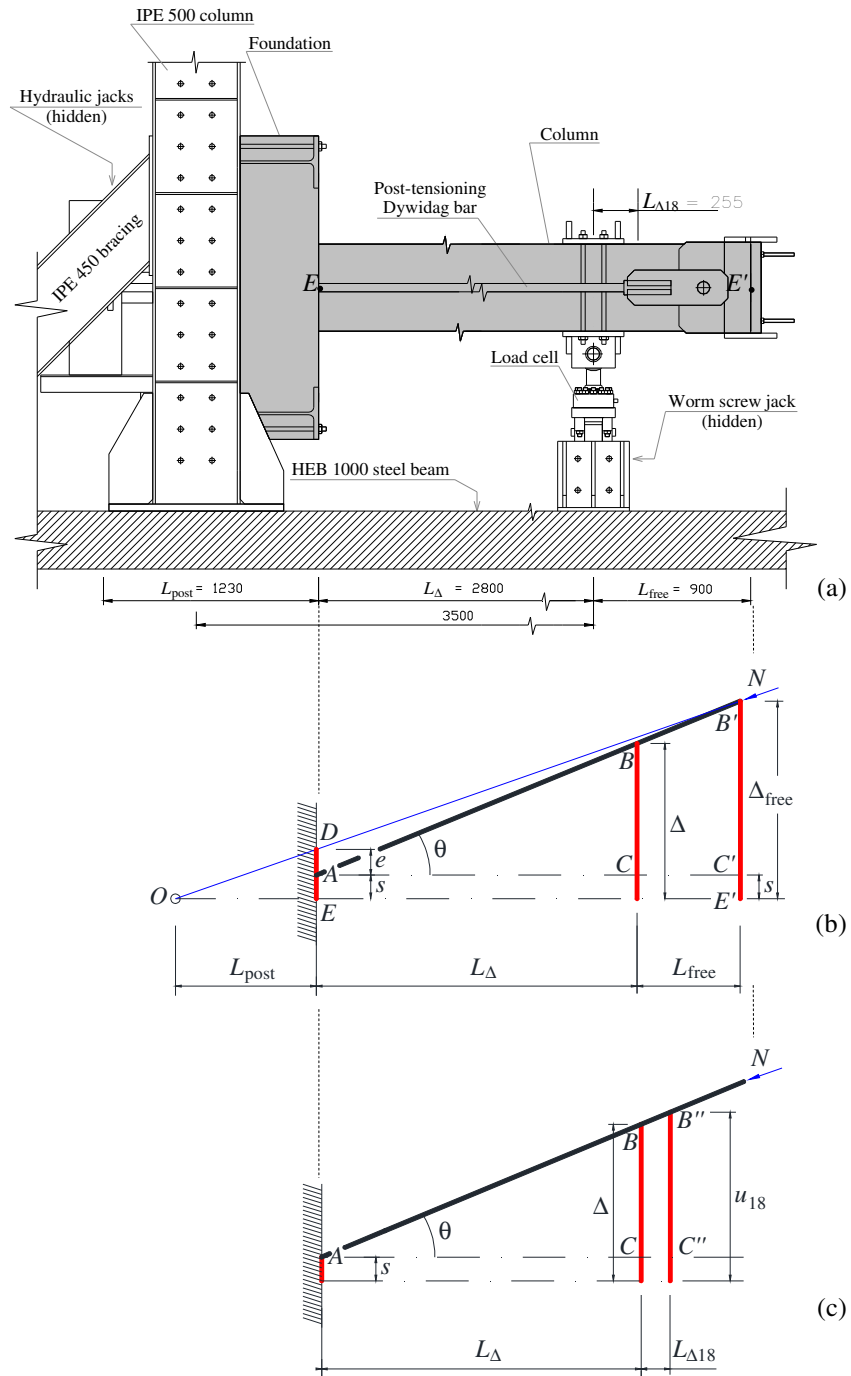- line *ODB′* indicates the direction of compressive axial load *N* at a generic test stage and coincides with the direction of the two Dywidag bars used for post-tensioning the column;

- Δ and Δ_{free} are the transverse deflections, referred to the column axis in the initial (undeformed) state, experienced by the cross-section where the cyclic actuator was acting and by the end section, respectively;

- $L_{\text{free}} = 0.9$ m is the distance between actuator and end section, whereas the line of application of *N* intersects the undeformed column axis behind the foundation, at a distance $L_{\text{post}} = 1.23$ m from the joint section.

Similarity between triangles *ABC* and *AB′C′* yields (Fig. 5b):

$$(\Delta - s)/L_{\Delta} = (\Delta_{\text{free}} - s)/(L_{\Delta} + L_{\text{free}}) \tag{1}$$

and transverse deflection Δ may then be expressed as:

$$\Delta = s + L_{\Delta}(\Delta_{\text{free}} - s)/(L_{\Delta} + L_{\text{free}}) \tag{2}$$

In addition, similarity between triangles *ODE* and *OB′E′* yields:

$$(e + s)/L_{\text{post}} = \Delta_{\text{free}}/(L_{\text{post}} + L_{\Delta} + L_{\text{free}}) \tag{3}$$

leading to the following expression for Δ_{free} in terms of *e* and *s*:

$$\Delta_{\text{free}} = L(e + s)/L_{\text{post}} \tag{4}$$

where $L = L_{\text{post}} + L_{\Delta} + L_{\text{free}}$. Solving Eq. (4) for *e* yields:

$$e = L_{\text{post}}\Delta_{\text{free}}/L - s \tag{5}$$

In similar experimental researches available in the literature the interface slip is not considered (PEER 2004, Verderame et al. 2008a), resulting, at equal Δ_{free}, in an axial load eccentricity higher than predicted by Eq. (5). Therefore, the presence of slip reduces the influence of second order effects. Substituting Eq. (4) into Eq. (2) leads to:

$$\Delta = s + [eL + (L_{\Delta} + L_{\text{free}})s]/[L_{\text{post}}(1 + L_{\text{free}}/L_{\Delta})] \tag{6}$$

The interface slip also influences the drift, which is computed as:

$$\theta = (\Delta - s)/L_\Delta \tag{7}$$

In analogy to what is done by PEER Center (2004) and Verderame et al. (2008a, b), an effective force taking account of second order effects is defined as:

$$F = F_\Delta - F_{\Delta 0} + Ne/L_\Delta \tag{8}$$

where F_Δ indicates the transverse force applied by the cyclic actuator and $F_{\Delta 0}$ is a correction term depending on the specimen self weight. This term, which was estimated based on the vertical reaction of an ideal constraint placed at distance L_Δ from the joint section, takes the values $F_{\Delta 0} = 15.8$ kN for the specimen being in the linear elastic range and $F_{\Delta 0} = 17.5$ kN after the formation of a plastic hinge at the column-to-foundation connection.

The experimental results will be presented in Section 4.4 in terms of F-Δ response, in accordance with several of the results collected in PEER Center's database (PEER 2004).

4.2. Loading protocol

The specimen was initially subjected to a compressive axial force $N = 1700$ kN in the absence of transverse load. This force corresponds to $0.14 f_{cm} A_c$, where $A_c = 2.40 \times 10^5$ mm^2 is the area of the concrete cross-section and $f_{cm} = 50.9$ MPa is the mean cylinder strength of concrete estimated as $\lambda f_{cm,cube}$, with $f_{cm,cube} = 61.3$ MPa (Table 1) and $\lambda = f_{cm}/f_{cm,cube} = 0.83$ in analogy with the ratio between the characteristic strengths recommended by the Italian standard (IMIT 2018).

With the axial compression kept constant, a cyclic transverse load was applied to the column at a distance L_Δ from the joint section in displacement control mode. The stroke rate was of 0.7 mm/min. The transverse loading protocol used in the test is graphically represented in Fig. 6 by a thin solid line (labeled "Δ"). The corresponding drift values are reported on the right vertical axis.

A total of 19 loading cycles were carried out. The first 10 cycles were intended not to damage the specimen. Their five target drifts were, in the order of their application, ±0.1%, ±0.2%, ±0.5%, ±0.7% and ±0.8%, each one repeated once (ACI 2013). Then, 8 cycles were carried out with target

drifts gradually increasing from 1% to 5%, with a step of 0.5% at each cycle. In the last cycle, the maximum attained drift was 5.3% (see Section 4.4). Therefore, 7 and 3 loading cycles were carried out with target drifts exceeding the allowable drifts defined by FEMA (2000) for Life Safety (2%) and Collapse Prevention (4%) performance levels, respectively.
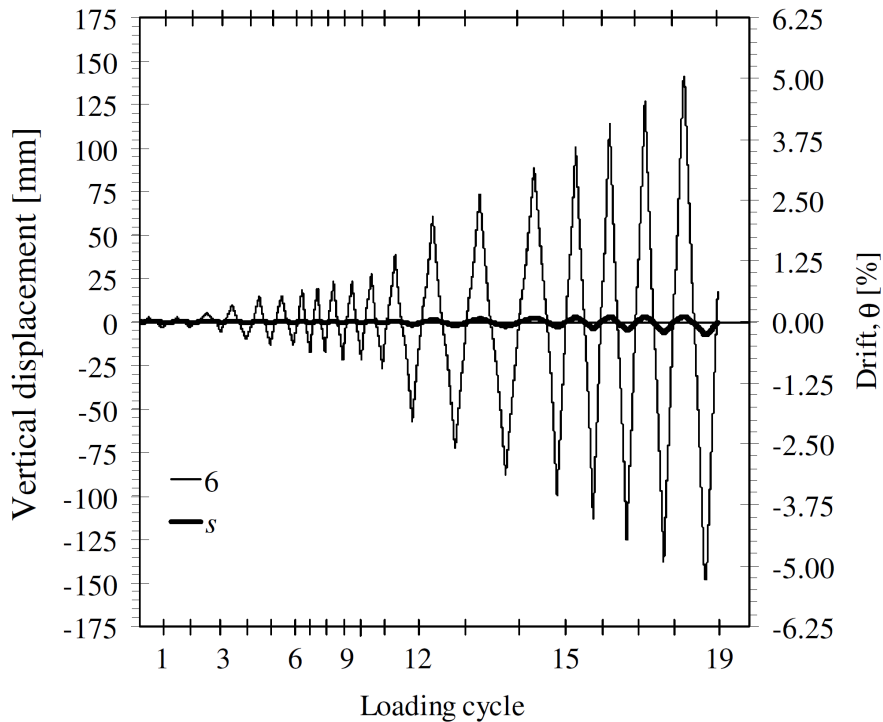

Fig. 6 Loading protocol in terms of deflection (Δ) of the column cross-section located at L_Δ from the joint section, and interface slip (s) during the test

4.3. Testing equipment and measuring system

The test rig (Fig. 4) is comprised of two HEB 1000 steel beams (whose top flanges are visible in Fig. 4a) accommodated into a specific compartment located below the pavement level and a 3.5m-high plane frame bolted to the beam top flanges. This frame, constituted by two IPE 500 columns and two HEB 400 beams, is stiffened by two IPE 450 inclined bracings against out-of-plane deformations. To place the specimen on the reaction frame, the two HEB 500 steel beams enclosing the foundation were connected to the HEB 400 profiles of the frame using twelve 27 mm-diameter threaded rods (some of which shown on top right and top left of Figs. 4a and 4c, respectively).

4.3.1. Application and measurement of the axial load

The column axial load was applied by post-tensioning two 47 mm-diameter Dywidag bars arranged parallel to the vertical sides of the column (Fig. 4a). At the column end section, each of these bars was screwed to a steel fork, which, in turn, was hinged to a lid anchored to the column tip. At the opposite side, behind the foundation, the Dywidag bars were connected to a suitable anchoring element by means of 83 mm-diameter threaded sleeves.

A detail view showing one of the Dywidag bars passing through the foundation is reported in Fig. 4b. Note that, for each bar, two switches were used to warn if the hole's boundary had been excessively approached by the bar due to column deflection.

The posterior anchoring system is shown in Fig. 4c. Also shown in the figure are the two hydraulic jacks with the loading capacity of 1 MN used for post-tensioning the Dywidag bars. These jacks, connected in parallel to the same pump, were positioned with the base against a load transfer steel element in contact with the posterior surface of the foundation and the plunger acting on the anchoring element for the Dywidag bars.

The pressure in the oleodynamic circuit activating the jacks was measured using pressure transducers with the nominal capacity of 700 bar. Being the two jacks identical, the axial load was obtained as twice the product of the measured pressure times the cylinder effective area of one jack, which was declared by the manufacturer.

4.3.2. Application and measurement of the cyclic transverse force

The vertical deflection time-history was applied by an electromechanical worm screw jack with loading capacity of 500 kN, stroke of ±250 mm and maximum rate of 0.7 mm/s, accommodated into a steel supporting element bolted to the HEB 1000 beams of the reaction frame (Fig. 4a). A Pi-shaped steel element, pinned to the jack, was used to support a 500 kN full-scale load cell with the nominal sensitivity of 2 mV/V (Fig. 4d). The cyclic force was transferred to the column by means of two stiffened steel plates positioned on the top and bottom sides.

4.3.3. Measurement of displacements and strains

Grouted bars in ducts may experience a significant slip under both monotonic and cyclic loading (Raynor et al. 2002). With regard to the bending tests presented by Tullini and Minghini (2016), the mismatch between measured and estimated strains in the projecting bars was ascribed to the slip of these bars with respect to the surrounding concrete. Similarly, a certain amount of bar slip was expected for the column-to-foundation connection presented in this paper. The detection of this slip would require applying strain gauges to both projecting bars and metal ducts along the entire lap length, with possible detrimental effects on the bond strength of the bars. Hence, in order not to alter the bond conditions within the lap splice, it was chosen to apply strain gauges to neither column bars nor corrugated ducts. Eighteen linear displacement transducers, in the following referred to as Li ($i = 1, ..., 18$), were used instead to measure absolute and relative displacements (Fig. 7).

With regard to the measurement of absolute displacements, seven transducers were used (in blue in Fig. 7a). Rigid body displacements of the specimen due to deformations of the reaction frame were measured by horizontal transducers L11 to L14 and vertical transducers L15 and L16. Transducers L11 to L16 are also shown in the frontal view of Fig. 7c. The same figure shows proximity switches S1 to S4 used to alert for an excessive approach of the Dywidag bars to the holes' boundaries. Transducer L18 (also shown in Fig. 4d) was used to measure the column vertical deflection (u_{18} in Fig. 5c) experienced by the cross-section located at a distance $L_\Delta + L_{\Delta 18} = 2800 + 255 = 3055$ mm from the joint section (Fig. 7a). In Fig. 5c, the same assumptions already adopted in Fig. 5b are used. In particular, straight line ABB'' indicates the column axis at the generic test stage. For simplicity, the line of application of N is not shown in this case. From similarity between triangles ABC and $AB''C''$ in Fig. 5c, deflection Δ turns out to be related with L18 measurements by the relation:

$$\Delta = s + L_\Delta \left(u_{18} - s \right) / \left(L_\Delta + L_{\Delta 18} \right) \tag{9}$$
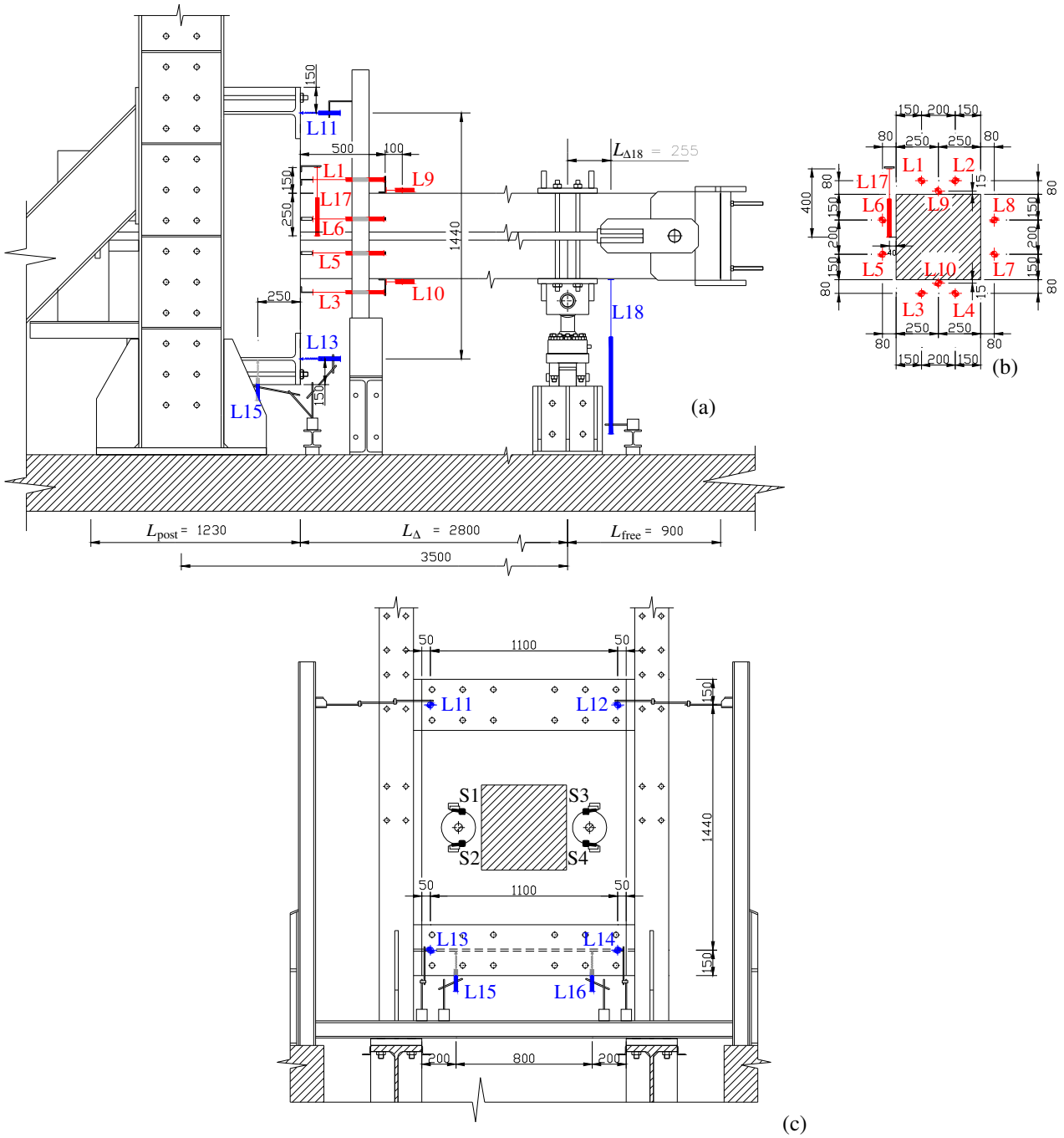
Fig. 7 Positions of the linear displacement transducers: (a) side view, (b) column cross-sectional view and (c) frontal view of the test setup. Dimensions in mm

All these transducers were attached, using magnets, to metal supports placed on the pavement of the laboratory, and therefore independent of the reaction frame.

With regard to the measurement of relative displacements, eleven transducers were used (in red in Fig. 7). Horizontal transducers L1 to L8 were positioned in proximity of the joint section as

shown in Figs. 4b and 7a, b, i.e., two transducers for each column side, placed in correspondence of the grouted ducts. These transducers were used to measure average strains in the column region where plastic hinge formation was expected. Other two horizontal transducers, i.e., L9 and L10, were positioned at the column top and bottom sides, respectively, to measure average strains near the joint section but outside the plastic hinge region. For each of these transducers, the average strain was estimated from the following relation ($i = 1, ..., 10$):

$$\varepsilon_i = u_i / b_i \tag{10}$$

where u_i is the displacement measured by the generic, i-th transducer and b_i represents the initial (undeformed) distance between the two points corresponding to the connections of transducer Li to the specimen. According with Fig. 7a, $b_i = 500$ mm for $i = 1, ..., 8$ and $b_i = 100$ mm for $i = 9$ and 10. Vertical displacement transducer L17 was used to measure the shear slip between column and foundation at the joint section, associated with the shear deformation of the projecting bars.

All displacement transducers, as well as pressure transducers (see § 4.3.1) and load cell (§ 4.3.2), were connected with the data acquisition system via a power unit operating at 50 mA and 10 V. A LabVIEW code (NI 2015) was developed to display all measurements in real-time.

4.4. Experimental results

The $F_\Delta-\Delta$ experimental diagram, with F_Δ (see Eq. (8)) being the cyclic transverse force applied by the actuator not including the correction terms for specimen self weight ($F_{\Delta 0}$) and second order effects (Ne/L_Δ), is reported in blue in Fig. 8a. The non-symmetry of the plot is due to the horizontal configuration of the specimen. To deflect the column upward, indeed, the actuator must contrast the self weight. Conversely, when the column deflects downward F_Δ and $F_{\Delta 0}$ take the same sign. This explains why the maximum absolute value of F_Δ attained during the downward half-cycles (negative force values) is approximately 18% smaller than that attained upward (positive force values).
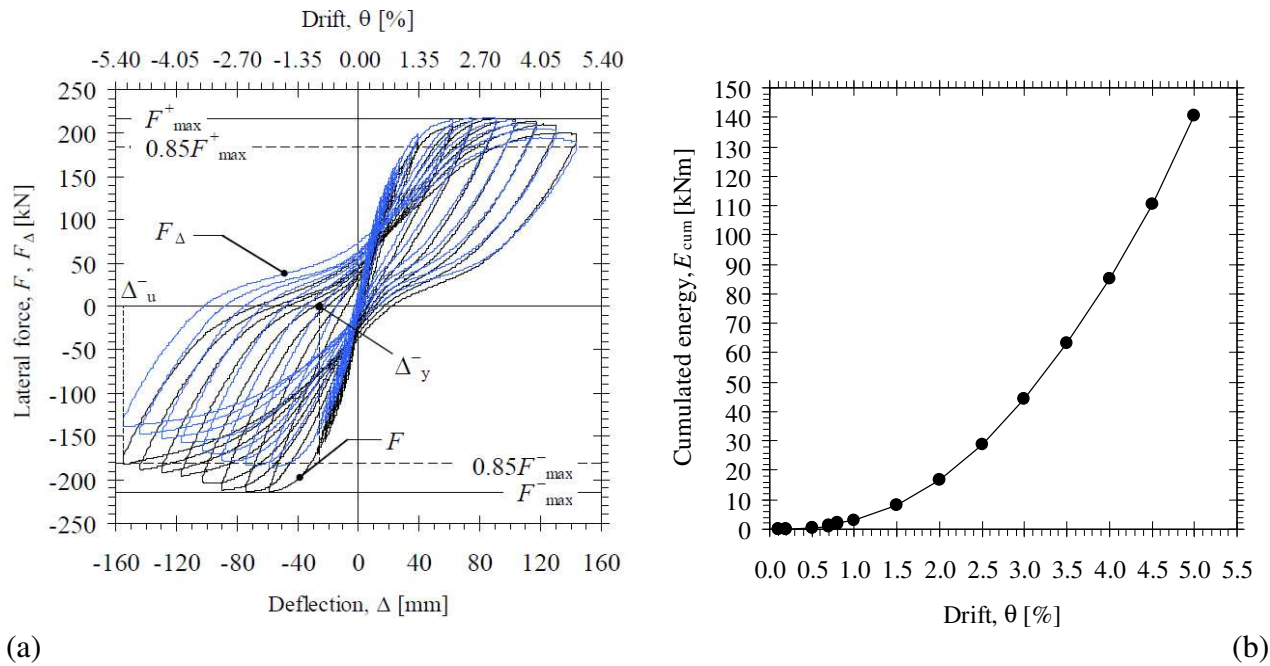
Fig. 8 Test results: (a) cyclic diagrams of applied (F_Δ) and effective (F) forces versus deflection and drift, and (b) cumulated hysteretic energy for the connection versus drift

The cyclic diagram shown in Fig. 8a with a black solid line refers instead to the $F-\Delta$ response of the specimen. It is again worth noting that force F, obtained from Eq. (8), includes both second order contribution and correction for self weight, and is therefore representative of the total bending resistance of the joint section (see Eq. (11)). As expected, due to the symmetry of the joint section (see cross-section B-B in Fig. 2), the F-Δ plot is substantially symmetric with respect to the origin. The softening effect observed in the F-Δ plot indicates a deterioration of the bending strength mainly related with the spalling of the concrete cover in the column.

The maximum effective force resisted by the column-to-foundation connection was $F_{max} = 216.2$ kN. The test was stopped at the end of the 19th loading cycle, in which the strength attained the value $F_u = 182.0$ kN $= 0.85 F_{max}$, where index "u" stands for ultimate. A resistance drop of 15% with respect to the peak strength corresponds indeed to one of the Ultimate Limit State (ULS) conditions stated by CEN (2004b). The maximum recorded values of deflection and slip were $\Delta_u = 155.1$ mm and $s_u = 7.3$ mm, respectively, resulting in drift $\theta_u = 5.3\%$. As is shown in Fig.

6, where the shear slip at the column-foundation interface is compared with vertical deflection, s started to develop for drifts larger than 2%.

The deflected configuration of the specimen during the last downward half-cycle is shown in Fig. 9a. In analogy with several experimental tests on precast column-to-foundation connections (Ameli et al. 2016; Belleri and Riva 2012; Dal Lago et al. 2016), the damage was mainly localized in proximity of the joint section, where yielding and hardening of the projecting bars were attained and complete spalling of the concrete cover took place on the column bottom (Fig. 9b) and top sides (Fig. 9c). Due to the confinement provided by the stirrups on the concrete core along the splice region and by the corrugated ducts on the inside grout, instability of the longitudinal reinforcement did not occur.

A video of the test (velocity increased 100 times) is provided, attached to the electronic version of the present paper to which the interested reader is referred to.

(a)   (b)   (c)

Fig. 9 (a) Column deflected configuration during the last half-cycle; and (b) bottom and (c) top sides of the column in proximity of the joint section at the end of test

4.4.1. Dissipated energy

The hysteretic energy (E_{hys}) dissipated during the test is defined as the area inside the experimental F-Δ cycles and may be estimated by applying the trapezoidal rule to the plot of Fig. 8a. The cumulated hysteretic energy, which for the generic, kth cycle is defined as $E_{cum,k} = \sum_{i=1}^{k} E_{hys,i}$, is reported in Fig. 8b versus drift. At the end of test ($\theta = \theta_u = 5.3\%$), $E_{cum} = 140$ kNm was achieved. The amount of dissipated energy strongly depends on the loading protocol adopted. The last 13 cycles of the displacement history shown in Fig. 6 are similar to the loading protocol used by Popa et al. (2015), comprised of 13 cycles at a drift ranging between 0.5% and 5%. The cumulated energy $E_{cum} = 140$ kNm is quite close to those reported by Popa et al. (2015) for cast-in-place specimen CIP2. Such a comparison is believed to be particularly meaningful, because specimen CIP2 showed almost the same transverse load capacity (about 200 kN) as the present specimen.

Although a certain tendency to pinching is shown in the F-Δ plot of Fig. 8a, the proposed connection presents a stable hysteretic behavior.

4.4.2. Moment-average curvature diagram for the joint section

The bending moment at the joint section, accounting for the second order effects, is given by the following equation:

$$M_j = FL_\Delta \tag{11}$$

with F being the effective transverse force obtained from Eq. (8). According with the positions of transducers reported in Fig. 7b, the average curvature may be evaluated, under the plain section hypothesis, from the following relation:

$$\chi_{j,A} = (\varepsilon_{34} - \varepsilon_{12})/d_A \tag{12}$$

or from the alternative relation:

$$\chi_{j,B} = (\varepsilon_{57} - \varepsilon_{68})/d_B \tag{13}$$

where ε_{12}, ε_{34}, ε_{57} and ε_{68} are the mean values of average strains obtained from Eq. (10) for the following pairs of displacement transducers: (L1, L2); (L3, L4); (L5, L7); and (L6, L8), respectively. Quantities $d_A = 660$ mm and $d_B = 200$ mm (Fig. 7b) are the vertical distances between transducers L1 and L3 (or, equivalently, L2 and L4), and between transducers L5 and L6 (or, equivalently, L7 and L8), respectively.

Average strain in the top layer (subscript 't') of projecting bars may be evaluated from the following alternative equations:

$$\varepsilon_{stA} = \varepsilon_{12} + \chi_{j,A} d_{stA} \tag{14}$$

$$\varepsilon_{stB} = \varepsilon_{68} - \chi_{j,B} d_{stB} \tag{15}$$

where $d_{stA} = 160$ mm and $d_{stB} = 70$ mm are the distances between top projecting bars and pairs of displacement transducers (L1, L2) and (L6, L8), respectively. Similarly, average strain in the bottom layer (subscript 'b') of projecting bars may be written as:

$$\varepsilon_{sbA} = \varepsilon_{12} + \chi_{j,A} d_{sbA} \tag{16}$$

$$\varepsilon_{sbB} = \varepsilon_{68} + \chi_{j,B} d_{sbB} \tag{17}$$

where $d_{sbA} = 500$ mm and $d_{sbB} = 270$ mm are the distances between bottom projecting bars and pairs of transducers (L1, L2) and (L6, L8), respectively.

Average concrete strains follow from similar relationships. For example, the strain at the top side of the column is given by:

$$\varepsilon_{ctA} = \varepsilon_{12} + \chi_{j,A} d_{ctA} \tag{18}$$

$$\varepsilon_{ctB} = \varepsilon_{68} - \chi_{j,B} d_{ctB} \tag{19}$$

whereas the strain experienced by the bottom side may be written as:

$$\varepsilon_{cbA} = \varepsilon_{12} + \chi_{j,A} d_{cbA} \tag{20}$$

$$\varepsilon_{cbB} = \varepsilon_{68} + \chi_{j,B} d_{cbB} \tag{21}$$

where (Fig. 7b) $d_{ctA} = 80$ mm, $d_{ctB} = 150$ mm, $d_{cbA} = 580$ mm and $d_{cbB} = 350$ mm.

Equations (12) and (13) led to substantially coincident curvature values. Therefore, the curvature at the joint section will be hereinafter defined as the average between $\chi_{j,A}$ and $\chi_{j,B}$ and simply referred to as χ_j. At the same time, average bar and concrete strains will be defined as $\varepsilon_{st} = (\varepsilon_{stA} + \varepsilon_{stB})/2$, $\varepsilon_{sb} = (\varepsilon_{sbA} + \varepsilon_{sbB})/2$, $\varepsilon_{ct} = (\varepsilon_{ctA} + \varepsilon_{ctB})/2$ and $\varepsilon_{cb} = (\varepsilon_{cbA} + \varepsilon_{cbB})/2$.

The records of displacement transducers L1 to L8 were also used to estimate the average column curvature in the horizontal plane, $\chi_{j\perp}$, produced by an unintended out-of-verticality of the applied transverse force. Yet, curvature $\chi_{j\perp}$ always remained one order of magnitude smaller than curvature χ_j.

Average strains ε_{st} and ε_{sb} in the projecting bars are reported in Fig. 10 versus deflection (units in the plot: ‰). The maximum tensile strain, attained during the last downward half-cycle, was $\varepsilon_{st} = 2.84\%$. According with Table 2, the mean value of the yield strain for the 20 mm-diameter bars is $\varepsilon_{ym} = 0.28\%$. The first yielding condition occurs when the outer layers of longitudinal reinforcement first attain strain ε_{ym}. Based on measurements of displacement transducers positioned in proximity of the joint section, the first yielding was detected during the 11th loading cycle in correspondence of deflection $\Delta_y = 25.3$ mm and effective force $F_y = 163.1$ kN. Therefore, the displacement ductility resulted to be $\mu_\Delta = \Delta_u/\Delta_y = 6.2$.

Also reported in Fig. 10 are negative values of strains ε_{ct} and ε_{cb} at top and bottom column sides. Obviously these strains represent a measure of actual compressive concrete strains only up to the spalling of the concrete cover. After spalling (Fig. 9b, c) the maximum compressive strains must be referred to the confined concrete core. For example, with regard to the concrete core dimensions reported in the Appendix, bottom concrete strain may still be written in the form of Eqs. (20)-(21), provided that distances d_{cbA} and d_{cbB} are replaced with $d_{ccbA} = d_{cbA} - (H - h_0)/2 = 534$ mm and $d_{ccbB} = d_{cbB} - (H - h_0)/2 = 304$ mm, respectively. With these substitutions, the maximum compressive strain at the bottom of the confined core, obtained from the average between Eqs. (20) and (21),

resulted to be 1.35%, i.e., approximately 4 times larger than the conventional ultimate strain for unconfined concrete, equal to 0.35%.
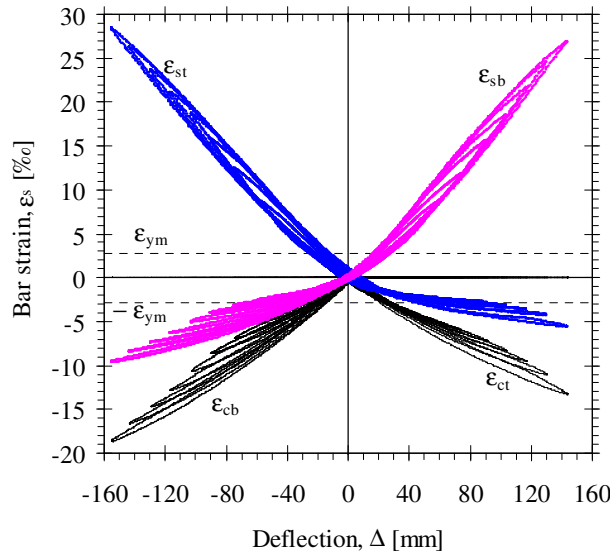

Fig. 10 Joint section deformability: average strains in top (ε_{st}) and bottom (ε_{sb}) projecting bars and average concrete compressive strains at top (ε_{ct}) and bottom (ε_{cb}) column sides
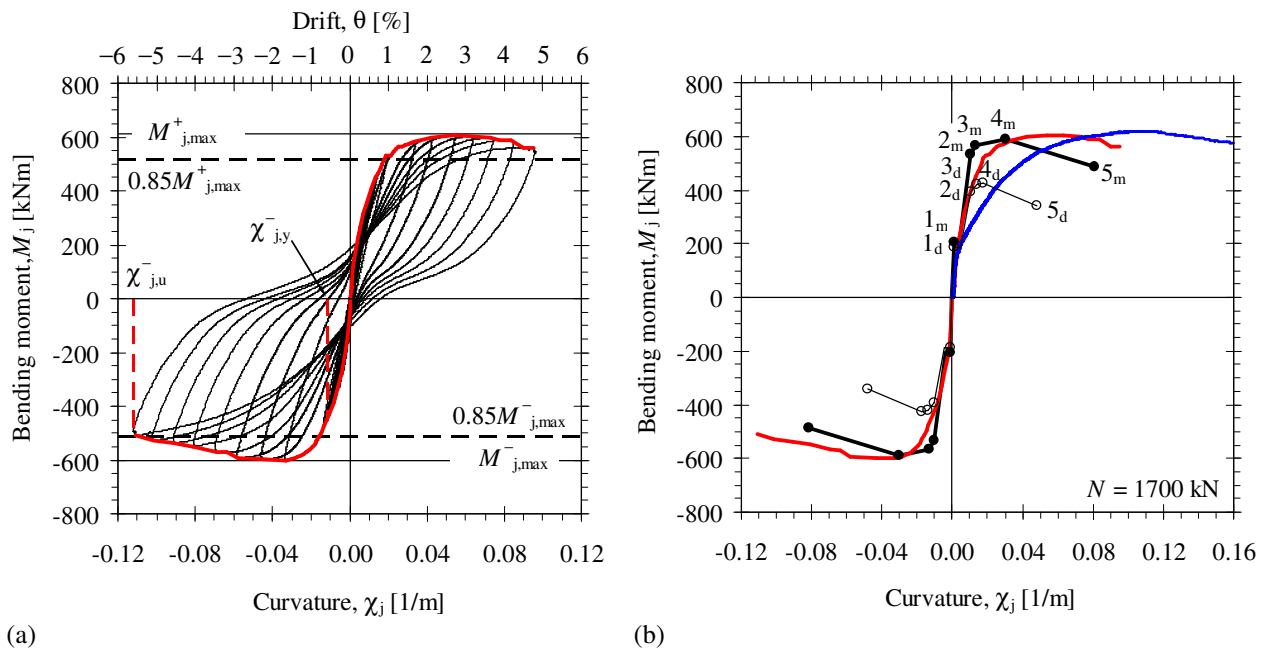
Fig. 11 Bending moment resisted by the joint section: (a) experimental cyclic diagram of moment versus curvature and drift; and (b) analytical moment-curvature diagrams for mean (thick black line) and design values (thin black line) of material properties. Computed values χ_{ja}, M_{ja} for solid and open circle data points in (b) are reported in Table 3. Red curve in the two figures represents the envelope diagram of the cyclic response. Blue line in (b) represents the experimental diagram obtained by Tullini and Minghini (2016) from a monotonic test

The cyclic diagram of bending moment M_j versus average curvature χ_j and drift θ is reported in Fig. 11a. Also reported in the same figure is the envelope of the hysteresis loops (red solid line). The maximum bending moment resisted by the joint section, i.e., $M_{j,max} = F_{max}L_\Delta = 605.4$ kNm, was obtained in correspondence of curvature $\chi_{j,max} = 0.0542$ m^{-1}. At the conventional ULS, i.e., for $M_{j,u} = 0.85F_{max}L_\Delta = 514.6$ kNm, average curvature was $\chi_{j,u} = 0.1119$ m^{-1}. The first yielding average curvature was $\chi_{j,y} = 0.0126$ m^{-1}. Therefore, the curvature ductility of the joint section resulted to be $\mu_{\chi j} = \chi_{j,u}/\chi_{j,y} = 8.9$.

The envelope diagram is reported again in Fig. 11b, where a comparison with the test in monotonic bending combined with axial compression described by Tullini and Minghini (2016) (blue line) is presented. The compressive axial force used in that investigation was approximately the same as in the present case. The maximum bending resistance of the monotonic response was only 2.3% larger than that of the cyclic response. This very small difference may be due to different material properties for the two specimens rather than to the influence of cyclic loading. The most significant feature of the comparison is the very greater flexural deformability shown by the monotonic case, which is evident starting from cracking. Tullini and Minghini (2016) ascribed this deformability to the slip between grouted bars and surrounding concrete, leading to a maximum recorded tensile strain in the projecting bars approximately 70% larger than predicted by section analysis. It is worth noting that also Raynor et al. (2002) shown that monotonically loaded bars in ducts may exhibit larger slip values in comparison with bars subjected to cyclic loading, not only in the post peak response but also in the proximity of bar yielding.

5. DISCUSSION

The analytical moment-curvature diagram for the joint section (subscript 'a', in the following, will indicate analytical quantities), evaluated by using the mean values of material properties, is

compared in Fig. 11b (thick black line) with the envelope diagram already reported in Fig. 11a, showing a satisfactory agreement.

In evaluating that diagram, concrete cracking strength $f_{ctm} = 3.7$ MPa computed according to Eurocode 2 (CEN 2004a) was used (point 1_m). A parabola-rectangle constitutive relationship, with cylindrical strength $f_{cm} = 50.9$ MPa (see Sect. 4.2), was adopted for concrete in compression (points 2_m to 4_m). The final descending branch was obtained by modifying geometry and properties of the concrete section. After the attainment of the peak flexural resistance (point 4_m), the concrete cover was considered to be removed from the column cross-section and increased compressive strength and strains were defined for the confined core inside the stirrups, leading to point 5_m. Increased concrete strength, f_{ccm}, strain at the attainment of the peak strength, ε_{c2c}, and ultimate strain, ε_{cu2c}, were estimated using Eqs. 3.24, 3.26 and 3.27, respectively, reported in Eurocode 2 (CEN 2004a). The effective lateral compressive stress due to confinement, appearing in those equations, was estimated from $\sigma = \alpha\sigma_0$ (CEB 1998), with σ_0 and α being ideal, uniformly distributed confining stress and confinement effectiveness factor, respectively. The procedure used for the calculation of point 5_m is detailed in the Appendix.

For the longitudinal reinforcing steel, an elastic-plastic relationship with linear hardening was adopted. The mean values for Young's modulus, yield and ultimate strengths, and ultimate strain for the projecting bars were deduced from the results of tension tests (Table 2).

Moment and curvature values corresponding to solid circle data points 1_m to 5_m in Fig. 11b are given in Table 3 together with tensile strain in the outer reinforcement layer (ε_{sa}) and effective force (F_a). Computed maximum and ultimate bending moments, $M_{ja,max} = 589$ kNm and $M_{ja,u} = 487$ kNm, are only 2.7% and 4.5% lower, respectively, than the corresponding experimental values. The computed maximum bar strain, $\varepsilon_{sa,max} = 2.22\%$, is 21.8% lower than the maximum average bar strain recorded during the test. This difference indicates that also in this test the grouted bars experienced a certain amount of slip within the ducts. Computed curvature ductility, $\mu_{\chi ja} = 7.8$ (see the Appendix), is 12.5% lower than that obtained from test.

Table 3 Computed responses of the joint section for mean (subscript 'm') and design (subscript 'd') values of material properties: tensile strain in the outer reinforcement layer (ε_{sa}), curvature (χ_{ja}), bending moment (M_{ja}) and effective force (F_a)

Computed quantity	Unit	Points of M_{ja}-χ_{ja} diagrams									
		Cracking		1st yielding[a]		2nd yielding[b]		Peak strength		Ultimate strength	
		1_m	1_d	2_m	2_d	3_m	3_d	4_m	4_d	5_m	5_d
ε_{sa}	[‰]	0.01	0.00	2.81	1.96	3.75	2.94	9.14	3.85	22.18	9.31
χ_{ja}	[‰/m]	1.13	1.06	10.4	10.1	13.4	14.1	30.1	17.5	81.2	48.1
M_{ja}	[kNm]	222	205	534	395	568	422	589	425	487	340
F_a	[kN]	79	73	191	141	203	151	210	152	174	122

Notes:

[a] 1st yielding refers to the achievement of yielding in tension for the outer bars;

[b] 2nd yielding refers to the achievement of yielding in tension for the bars located at 350 mm from the most compressed fibre.

Also reported in Fig. 11b (thin black line) is the analytical moment-curvature diagram for the joint section evaluated by using the design values of material properties. Concrete strength class C40/50 was adopted (see Sect. 3.1). For concrete in tension, cracking strength $f_{ctd} = 2.9$ MPa, obtained from the Italian standard (IMIT 2018), was used (point 1_d). For concrete in compression, a parabola-rectangle relationship with $f_{cd} = \alpha_{cc}f_{ck}/\gamma_c = 22.7$ MPa (IMIT 2018) for the maximum compressive strain ranging between $\varepsilon_{c2} = 0.20\%$ and $\varepsilon_{cu2} = 0.35\%$ was used (points 2_d to 4_d). After the attainment of the peak flexural resistance and concrete cover removal, increased properties were defined for the concrete core (see the Appendix), leading to point 5_d.

For the longitudinal reinforcing steel, an elastic-perfectly plastic relationship was adopted with $E = 200$ GPa, $f_{yd} = 391$ MPa and $\varepsilon_{td} = 6.75\%$ (IMIT 2018).

The values of ε_{sa}, χ_{ja}, M_{ja} and F_a corresponding to open circle data points 1_d to 5_d in Fig. 11b are given in Table 3. Design moment resistance results to be $M_{ja} = M_{Rd} = 425$ kNm (point 4_d). Thus, the connection system proposed exhibited an over-strength factor of $M_{j,max}/M_{Rd} = 1.42$, very close to the over-strength of 1.35 found by Tullini and Minghini (2016) in the test on a column-to-column joint subjected to monotonic bending combined with axial compression. Design curvature ductility is given by $\mu_{\chi ja} = 4.8$ (see the Appendix). Therefore, the gain in ductility exhibited by the connection system is 8.9/4.8 = 1.9.

The design bending strength of the column far away from the joint section (cross-section D-D in Fig. 2b) is only 4.5% larger than that of the joint section itself. This difference is essentially due to the different positions of bars within the relevant cross-sections. The use of projecting bars with a larger diameter in comparison with the regular reinforcing bars in the column would result in a greater strength for the joint than for the column. Anyway, the experimental connection strength still is 36% greater than the design strength of the column.

6. CONCLUSIONS

The connection system investigated, first proposed by Tullini and Minghini (2016), has the steel ducts positioned along the sides of the column cross-section. Therefore, differently from similar connections presented in the literature, in which the ducts are placed at the cross-section corners, this system allows for using traditional reinforcement cages for the column, with longitudinal bars at both mid-side and corners of the cross-section. The length of the lap splice between projecting bars and regular column bars was designed on the basis of the Eurocode 2 provisions for deformed bars (see Sections 8.4.2, 8.4.3 and 8.7.3 of Eurocode 2, CEN 2004a), neglecting the confinement effect provided by the ducts. The amount of transverse reinforcement along the splice region was defined to meet the requirements reported in Section 8.7.4 of Eurocode 2 (CEN 2004a). For the particular arrangement of 20 mm-diameter longitudinal bars shown in Fig. 1a, the minimum required lap length and the actual lap length resulted to be of 900 mm (45 $\varnothing_b$) and 1 m (50 $\varnothing_b$), respectively. The transverse reinforcement along the splice was comprised of 8 mm-diameter square and diamond-shaped stirrups every 100 mm. Due to the bars positions, the design bending strength of the column far away from the joint section is 4.5% larger than that of the joint section itself.

The experimental programme initiated by Tullini and Minghini (2016) is completed in the present paper with a full-scale test in cyclic bending combined with an axial compression of 1700 kN, resulting in $\nu_d = 0.3$. Although the test results for only one precast specimen are presented here (as in the recent paper by Rave-Arango et al. 2018), the key response parameter for the connection

system are believed to be exhaustively described by gathering together the present findings and results obtained from Tullini and Minghini (2016).

The connection system, used here for a column-to-foundation joint, was subjected to 19 loading cycles achieving strength degradation and drift of 15% and 5.3%, respectively. Failure concentrated mainly at the joint section, where yielding and hardening of the projecting bars occurred. The shear slip at the column-foundation interface, activated by plasticization at the column base, led to a slight reduction of second order effects. The maximum measured slip was approximately 5% of the column deflection. Displacement and curvature ductilities obtained from test were 6.2 and 8.9, respectively. With respect to the design values of bending resistance and curvature ductility computed with the rules for traditional RC members, the joint section showed an over-strength factor of 1.4 and a gain in ductility of 87%. Given the effect of column aspect ratio L_Δ/H (i.e., shear span length over column cross-section depth) on failure mode and ductility, documented by some parametric analysis on cyclically loaded RC columns (Ying and Jin-Xin 2018), the remarkable ductility shown by the specimen described in this paper should be regarded with care when using the same connection system but with a different aspect ratio.

The dissipated energy was comparable with that reported by Popa et al. (2015) for a cast-in-place specimen pushed up to the same maximum drift and having approximately the same capacity as the specimen described in this paper.

Mazza for their contribution to the preparation of the experimental test, and to Dr. Massimo Vichi for the video editing.

APPENDIX

This appendix reports the lap splice design (Table 4) and calculation of concrete properties due to confinement (Tables 5 and 6). The confined concrete core characteristics are shown in Fig. 12.

Table 4 Design lap length for the longitudinal column reinforcement and transverse reinforcement requirements along the lap splice (CEN 2004a). The calculations assume concrete strength class C40/50

| Symbol, description [Units]		Equation/Condition/Fig.	Value
f_{ck}	Characteristic compressive strength for concrete [MPa]		40
$f_{ctk,0.05}$	Characteristic tensile strength for concrete [MPa]		2.50
γ_c	Partial safety factor for concrete [-]		1.50
f_{ctd}	Design tensile strength for concrete [MPa]	$f_{ctd} = f_{ctk,0.05}/\gamma_c$	1.67
f_{yk}	Characteristic yield strength for reinforcing steel [MPa]		450
γ_s	Partial safety factor for reinforcing steel [-]		1.15
f_{yd}	Design yield strength for reinforcing steel [MPa]	$f_{yd} = f_{yk}/\gamma_s$	391
$\varnothing_b$	Diameter of longitudinal reinforcement bars [mm]		20
$\varnothing_{st}$	Diameter of transverse reinforcement bars [mm]		8
η_1	Coefficient related to bond conditions and bar position during casting [-]	For poor bond condition	0.7
η_2	Coefficient related to longitudinal bar diameter [-]	For $\varnothing_b \leq 32$ mm	1.0
f_{bd}	Design ultimate bond stress for reinforcing bars in concrete [MPa]	$f_{bd} = 2.25\eta_1\eta_2 f_{ctd}$	2.63
$l_{b,rqd}$	Basic required anchorage length [mm]	$l_{b,rqd} = \varnothing_b f_{yd}/4 f_{bd}$	745
c_d	Minimum concrete cover for longitudinal bars [mm]		50
K	Coeff. related with the relative position of longit. and transv. bars [-]	Bar engaged by a stirrup corner (see Fig. 1a)	0.1
A_s	Area of a single spliced bar [mm^2]	$A_s = \pi\varnothing_b^2/4$	314
ΣA_{st}	Area of stirrups per each longit. bar along the anchorage length [mm^2]	$\Sigma A_{st} = 10\,\pi\varnothing_{st}^2/4$	503
$\Sigma A_{st,min}$	Area of the minimum transverse reinforcement [mm^2]	$\Sigma A_{st,min} = A_s$	314
λ	Coefficient related with the area of reinforcement [-]	$\lambda = (\Sigma A_{st} - \Sigma A_{st,min})/A_s$	0.60
ρ_1	Percentage of bars lapped at the column base [%]		100
d_{max}	Maximum clear distance between projecting and regular bars [mm]	See Fig. 1a	82
l_{add}	Additional lap length due to a d_{max} exceeding $4\varnothing_b$ or 50 mm [mm]	$l_{add} = d_{max}$	82
α_1	Coefficient accounting for bar shape [-]	For straight bar	1.00
α_{2t}	Coefficient accounting for concrete cover, bar in tension [-]	$\alpha_{2t} = 1 - 0.15(c_d - \varnothing_b)/\varnothing_b$	0.78
α_{2c}	Coefficient accounting for concrete cover, bar in compression [-]	For all types of anchorage	1.00
α_{3t}	Coefficient accounting for confinement, bar in tension [-]	$\alpha_{3t} = 1 - K\lambda$	0.94
α_{3c}	Coefficient accounting for confinement, bar in compression [-]	For all types of anchorage	1.00
α_5	Coefficient accounting for confinement by transverse pressure p [-]	For $p = 0$	1.00
α_{6t}	Coefficient accounting for the value of ρ_1, bar in tension [-]	For $\rho_1 \geq 50$	1.50
α_{6c}	Coefficient accounting for the value of ρ_1, bar in compression [-]	For all types of anchorage	1.00
l_{0t}	Design lap length in tension [mm]	$l_{0t} = \alpha_1\alpha_{2t}\alpha_{3t}\alpha_5\alpha_{6t}l_{b,rqd} + l_{add}$	897
l_{0c}	Design lap length in compression [mm]	$l_{0c} = \alpha_1\alpha_{2c}\alpha_{3c}\alpha_5\alpha_{6c}l_{b,rqd} + l_{add}$	828
l_0	Actual lap length [mm]	$l_0 \geq \max\{l_{0t}, l_{0c}\}$	1000
$\Sigma A_{st}/2$	Area of stirrups per each longit. bar in tension, to be placed at the outer sections of the lap within $l_0/3$ of the lap length [mm^2]	$\Sigma A_{st}/2 = 4\,\pi\varnothing_{st}^2/4 \geq A_s/2$ (see Fig. 2a)	201
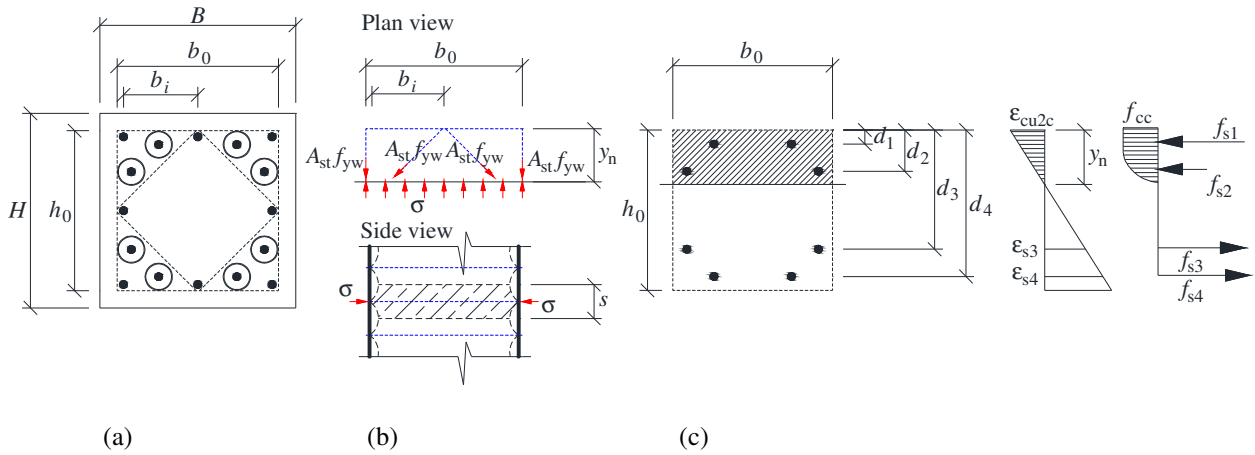
Fig. 12 Evaluation of the post-peak bending resistance for the joint section: (a) stirrups arrangement and positions of engaged bars; (b) equilibrium condition for the calculation of confining stress σ on the compressed concrete core and (c) effective cross-section with strain and stress diagrams

Table 5 Concrete core geometry and confinement effectiveness factor

Symbol, description [Units]		Equation	Value
$B = H$	Column cross-section dimensions [mm]		500
c	Clear concrete cover [mm]		42
$\varnothing_b$	Diameter of longitudinal reinforcement bars [mm]		20
$\varnothing_{st}$	Diameter of transverse reinforcement bars [mm]		8
n	No. of engaged bars (= No. of projecting bars) [mm]		8
s	Spacing of transverse reinforcement [mm]		100
d_{i0}	Distance of the i-th layer of projecting bars from the top [mm] Joint section in Fig. 2b ($i = 1, ..., 4$)		80; 150; 350; 420
A_s	Cross-sectional area of one longitudinal bar [mm²]	$A_s = \pi\varnothing_b^2/4$	314
A_{st}	Cross-sectional area of one leg of transverse reinforcement [mm²]	$A_{st} = \pi\varnothing_{st}^2/4$	50
$b_0 = h_0$	Dimensions of confined core (to the centreline of the stirrups) [mm]	$b_0 = B - 2c - \varnothing_{st}$	408
b_i	Distance between consecutive engaged bars [mm]	$b_i = 1/2\left(b_0 - \varnothing_{st} - \varnothing_b\right)$	190
d_i	Distance of the i-th layer of projecting bars from the top [mm] Joint section in Fig. 12c ($i = 1, ..., 4$)	$d_i = d_{i0} - c - \varnothing_{st}/2$	34; 104; 304; 374
α_n	Confinement factor, see CEB (1998) and CEN (2004b) [-]	$\alpha_n = 1 - \sum_{i=1}^{n} b_i^2/6b_0^2$	0.71
α_s	Confinement factor, see CEB (1998) and CEN (2004b) [-]	$\alpha_s = \left(1 - s/2b_0\right)^2$	0.77
α	Confinement effectiveness factor [-]	$\alpha = \alpha_n\alpha_s$	0.55

Table 6 Computed properties for confined concrete and curvature ductility. Subscripts 'm', 'k' and 'd' stand for mean, characteristic and design property, respectively

Symbol, description [Units]		Equation	Value $(\cdot)_m$	$(\cdot)_k$	$(\cdot)_d$
f_c	Unconfined concrete compressive strength [MPa]		50.9	40.0	22.7
f_{yw}	Yield strength of transverse reinforcement [MPa]		518	450	391
σ	Confining stress, see CEB (1998) [MPa]	$\sigma = \alpha A_{st} f_{yw}\left(2+\sqrt{2}\right)\big/ sb_0$	1.19	1.04	0.90
f_{cc}	Compressive strength for confined concrete, see CEB (2004a) [MPa]	$f_{cc} = f_c\left(1+5\sigma/f_c\right)$	56.8	45.2	25.6[a]
ε_{c2c}	Compressive strain at the attainment of peak strength for confined concrete, see CEB (2004a) [‰]	$\varepsilon_{c2c} = \varepsilon_{c2}\left(f_{cc}/f_c\right)^2$	2.50	2.55	
ε_{cu2c}	Ultimate compressive strain for confined concrete, see CEB (2004a) [‰]	$\varepsilon_{cu2c} = \varepsilon_{cu2} + 0.2\,\sigma/f_c$	8.19	8.68[b]	
y_n	Neutral axis depth [mm]	y_n from section analysis	100.8		180.4
f_{si}	Stress in projecting bars [MPa] Joint section in Fig. 12c (i = 1, ..., 4)	f_{si} from section analysis	−559; 51; 557; 576		−391; −391; 391; 391
χ_u	Ultimate curvature (see Table 3) [‰/m]	$\chi_u = \varepsilon_{cu2c}/y_n$	81.20		48.11
μ_χ	Curvature ductility [-]	$\mu_\chi = \chi_u/\chi_y$ [c]	7.80		4.76

Notes:

[a] Evaluated from $f_{ccd} = \alpha_{cc}f_{cck}/\gamma_c = 25.6$ MPa, where $\alpha_{cc} = 0.85$ and $\gamma_c = 1.5$;

[b] Evaluated for $\sigma = \sigma_k = 1.04$ MPa and $f_c = f_{ck} = 40.0$ MPa;

[c] 1st yielding curvatures $\chi_{ym} = 10.4$ ‰/m and $\chi_{yd} = 10.1$ ‰/m correspond to points 2_m and 2_d in Table 3.

REFERENCES

ACI (American Concrete Institute) (2013) ACI 374 – Guide for testing reinforced concrete structural elements under slowly applied simulated seismic loads, Farmington Hills, MI

Ameli MJ, Brown DN, Parks JE, Pantelides CP (2016) Seismic column-to-footing connections using grouted splice sleeves. ACI Structural Journal 113(5):1021-1030

Belleri A, Brunesi E, Nascimbene R, Pagani M, Riva P (2015) Seismic performance of precast industrial facilities following major earthquakes in the Italian territory. Journal of Performance of Constructed Facilities 29(5):04014135

Belleri A, Riva P (2012) Seismic performance and retrofit of precast concrete grouted sleeve connections. PCI Journal 57(1):97-109

Bruggeling ASG, Huyghe GF (1991) Prefabrication with Concrete. A. A. Balkema, Rotterdam

Buratti N, Bacci L, Mazzotti C (2014) Seismic behaviour of grouted sleeve connections between foundations and precast columns. In: Proceedings of the 2nd European Conference on Earthquake Engineering and Seismology. Istanbul, August 25-29

Buratti N, Minghini F, Ongaretto E, Savoia M, Tullini N (2017) Empirical seismic fragility for the precast RC industrial buildings damaged by the 2012 Emilia (Italy) earthquakes. Earthquake Engineering and Structural Dynamics 46(14):2317-2335

CEB (Euro-International Committee for Structural Concrete) (1998) CEB-FIP Model Code 1990 - Design Code, 2nd edn. Thomas Telford, London

CEN (European Committee for Standardization) (2004a) EN 1992-1-1:2004, Eurocode 2 – Design of concrete structures – Part 1-1: General rules and rules for buildings. CEN, Brussels

CEN (European Committee for Standardization) (2004b) EN 1998-1:2004, Eurocode 8 – Design of structures for earthquake resistance – Part 1: General rules, seismic actions and rules for buildings. CEN, Brussels

Dal Lago B, Toniolo G, Lamperti Tornaghi M (2016) Influence of different mechanical column-foundation connection devices on the seismic behaviour of precast structures. Bulletin of Earthquake Engineering 14(12):3485-3508

Demartino C, Vanzi I, Monti G, Sulpizio C (2018) Precast industrial buildings in Southern Europe: loss of support at frictional beam-to-column connections under seismic actions. Bulletin of Earthquake Engineering 16(1):259-294

Elliott KS (2017) Precast Concrete Structures, 2nd edn. CRC Press, Taylor & Francis Group, Boca Raton

FEMA (Federal Management Emergency Agency) (2000) FEMA 356 – Prestandard and commentary for the seismic rehabilitation of buildings. Washington, D.C.

FIB (International Federation for Structural Concrete) (2003) Seismic design of precast concrete building structures, Bulletin No. 27, FIB, Lausanne

Hua LJ, Rahman ABA, Ibrahim IS (2014) Feasibility study of grouted splice connector under tensile load. Construction and Building Materials 50:530-539

IMIT (Italian Ministry of Infrastructure and Transport) (2018) Italian Building Code-D.M. 17/01/2018, Rome [in Italian]

Kuttab AS, Dougill JW (1988) Grouted and dowelled jointed precast concrete columns - Behaviour in combined bending and compression. Magazine of Concrete Research 40(144):131-142

Liu Y, Zhou B, Cai J, Sang-Hoon Lee D, Deng X, Feng J (2018) Experimental study on seismic behavior of precast concrete column with grouted sleeve connections considering ratios of longitudinal reinforcement and stirrups. Bulletin of Earthquake Engineering, https://doi.org/10.1007/s10518-018-0414-9

Minghini F, Ongaretto E, Ligabue V, Savoia M, Tullini N (2016) Observational failure analysis of precast buildings after the 2012 Emilia earthquakes. Earthquakes and Structures 11(2):327-346

Negro P, Toniolo G (eds.) (2012) Design guidelines for connections of precast structures under seismic actions. EUR - Scientific and Technical Research Reports. JRC Publication No. JRC71599. Publications Office of the European Union, http://dx.doi.org/10.2777/37605

NI (National Instruments) (2015) LabVIEW 2015 Help. Available at http://www.ni.com/support. Accessed 23 February 2015

Park R (1988) Ductility evaluation from laboratory and analytical testing (State-of-the-Art Report). In: Proceedings of the 9th World Conference on Earthquake Engineering. Tokyo-Kyoto, August 2-9

Park R (1995) Perspective on the Seismic Design of Precast Concrete Structures in New Zealand. PCI Journal 40(3):40-60

PEER (Pacific Earthquake Engineering Research Center) (2004) Structural Performance Database User's manual, University of Berkeley. Available at https://nisee.berkeley.edu/spd/. Accessed 1 July 2018

Popa V, Papurcu A, Cotofana D, Pascu R (2015) Experimental testing on emulative connections for precast columns using grouted corrugated steel sleeves. Bulletin of Earthquake Engineering 13(8):2429-2447

Rave-Arango JF, Blandón CA, Restrepo JI, Carmona F (2018) Seismic performance of precast concrete column-to-column lap-splice connections. Engineering Structures 172:687-699

Raynor DJ, Lehman DE, Stanton JF (2002) Bond-slip response of reinforcing bars grouted in ducts. ACI Structural Journal 99(5):568-576

Savoia M, Buratti N, Vincenzi L (2017) Damages and collapses in industrial precast buildings after the 2012 Emilia earthquake. Engineering Structures 137:162-180

Sezen H, Whittaker AS (2006) Seismic performance of industrial facilities affected by the 1999 Turkey earthquake. Journal of Performance of Constructed Facilities 20(1):28-36

Toniolo G, Colombo A (2012) Precast concrete structures: The lessons learned from L'Aquila earthquake. Structural Concrete 13(2):73-83

Tullini N, Minghini F (2016) Grouted sleeve connections used in precast reinforced concrete construction - Experimental investigation of a column-to-column joint. Engineering Structures 127:784-803

Verderame GM, Fabbrocino G, Manfredi G (2008a) Seismic response of r.c. columns with smooth reinforcement. Part I: Monotonic tests. Engineering Structures 30(9):2277-2288

Verderame GM, Fabbrocino G, Manfredi G (2008b) Seismic response of r.c. columns with smooth reinforcement. Part II: Cyclic tests. Engineering Structures 30(9):2289-2300

Yan Q, Chen T, Xie Z (2018) Seismic experimental study on a precast concrete beam-column connection with grout sleeves. Engineering Structures 155:330-344

Yanev P (1989) Performance of industrial facilities. Earthquake Spectra 5(3):101-113

Yuan H, Zhenggeng Z, Naito CJ, Weijian Y (2017). Tensile behavior of half grouted sleeve connections: Experimental study and analytical modeling. Construction and Building Materials 152:96-104

Ying M, Jin-Xin G (2018) Seismic failure modes and deformation capacity of reinforced concrete columns under cyclic loads. Periodica Polytechnica Civil Engineering 62(1):80-91

Zheng LX (1996) Grouted precast concrete column connections under reversed cyclic bending and compression. ACI Structural Journal 93(3):247-256